

Pressure-Induced Superconductivity at 18.2 K in CuIr_2S_4

Bijuan Chen^{1,2,†,*}, Yuhao Gu³, Dong Wang¹, Dexi Shao^{3,10}, Wen Deng¹, Xin Han³, Meiling Jin⁴, Yu Zeng³, Hirofumi Ishii⁵, Yen-Fa Liao⁵, Dongzhou Zhang⁶, Jianbo Zhang¹, Youwen Long^{3,9}, Jinlong Zhu⁴, Liuxiang Yang¹, Hong Xiao¹, Jia-cai Nei⁷, Youguo Shi³, Changqing Jin³, Jiangping Hu^{3*}, Hengkang Mao^{1,8} and Yang Ding^{1*}

¹ Center for High-Pressure Science and Technology Advanced Research, Beijing, 100094, China

² Department of Physics, Harvard University, Cambridge, Massachusetts 02138, USA

³ Institute of Physics, Chinese Academy of Sciences, Beijing 100190, China

⁴ Department of Physics and Shenzhen Engineering Research Center for Frontier Materials Synthesis at High Pressures, Southern University of Science and Technology (SUSTech), Shenzhen 518055, China

⁵ National Synchrotron Radiation Research Center, Hsinchu 30076, Taiwan

⁶ Hawaii Institute of Geophysics & Planetology, University of Hawaii Manoa, Honolulu, Hawaii 96822, United States

⁷ Department of Physics, Beijing Normal University, Beijing 100875, China

⁸ Shanghai Advanced Research in Physical Sciences, Shanghai 201208, China

⁹ Songshan Lake Materials Laboratory, Dongguan, Guangdong 523808, China

¹⁰ Department of Physics, Hangzhou Normal University, Hangzhou 311121, China

ABSTRACT: Attaining superconducting critical temperatures (T_c) beyond the limit around 14 K observed thus far in spinel compounds AB_2X_4 (A, B = transition metals, X = O/chalcogen) could elucidate interaction intricacies and inform materials design. This work spotlights CuIr_2S_4 , which exhibits a distinct metal-insulator transition below 230 K, as an unconventional candidate for activation under high pressure. Through transport, diffraction, and spectroscopy experiments conducted at pressures up to 224 GPa, we unveil pressure-tuning that suppressed CuIr_2S_4 's transition, yielding two superconducting phases with an unprecedented T_c for spinels. Initially, 3.8 K onset rose monotonically, reaching 18.2 K at 133 GPa. Unexpectedly, a distinct phase with $T_c = 2.2$ K distinctly emerged at higher pressures, intimating unconventional couplings. Our findings suggest that both geometric frustration and electron-electron interactions play crucial roles in the superconductivity observed in CuIr_2S_4 . The findings stretch perceived temperature limits in spinels and provide structure-property insights to guide the optimization of quantum materials interactions for tailored targeted functionalities.

INTRODUCTION

Superconductivity, a cornerstone in condensed matter physics, holds immense potential for a diverse range of applications, from energy-efficient technologies to explorations in fundamental physics. The relentless pursuit of higher critical temperatures (T_c) in superconductors remains a central theme in this field, driven by both fundamental scientific curiosity and the promise of transformative applications. Spinel compounds (AB_2X_4 , where A and B are different transition metals and X is O or a chalcogen), have garnered significant attention due to their unique electronic properties, which arise from the intricate interplay of spin, charge, and orbital degrees of freedom¹⁻⁵. These properties can induce exotic emergent phenomena⁶⁻⁹, including metal-insulator transitions¹⁰⁻¹¹, magnetic order⁸, and notably, superconductivity (SC)¹²⁻¹³, making them promising candidates for various industrial and technological applications^{7,12-15}. The exotic properties of spinels usually stem from the electronic interactions' characteristic of, or geometrically frustrated magnetic in, the corner-sharing tetrahedral networks of B-site cations.

Well-known examples include charge ordering in CuIr_2S_4 ⁶ and Fe_3O_4 ⁴, spin fluctuations in ZnCr_2O_4 ⁵, and orbital ordering in MgTi_2O_4 ¹⁶. However, despite theoretical predictions and promising material properties, the T_c of reported spinel superconductors has remained capped at 13.7 K for decades^{15,17}.

Within this landscape, CuIr_2S_4 emerges as a particularly intriguing candidate, defying conventional expectations. CuIr_2S_4 has a cubic symmetry belonging to the group of $Fd\bar{3}m$, with a lattice parameter of $a = 9.847$ Å at room temperature with the metallic state¹⁰, where the Cu ion is tetrahedrally coordinated and the Ir ion is octahedrally coordinated by sulfur atoms, as shown in Figure 1A and Figure S1 in the Supplementary Information (SI). Remarkably, upon cooling, a metal-insulator transition (MIT) occurs below 230 K, accompanied by a distortion from a cu-

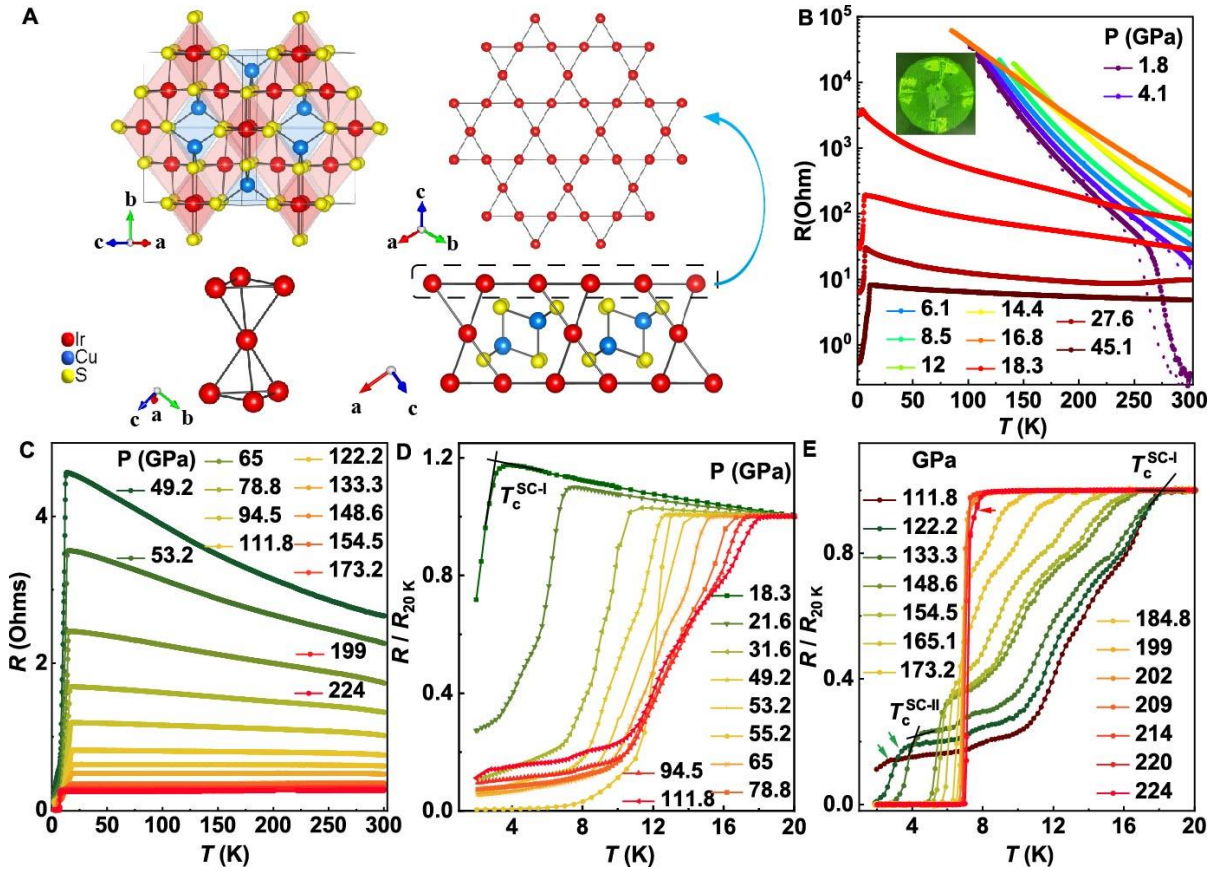


Figure 1. Structural characterization of 2H GeH at ambient pressure and pressure-induced superconductivity in CuIr_2S_4 . (A) The crystal structure of the CuIr_2S_4 . The Ir sublattice forms a network of corner-sharing tetrahedra and a perfect 2D Kagome-like¹⁸ net. (B and C) Temperature dependence of resistance of CuIr_2S_4 under various pressures up to 224 GPa. (D and E) An expanded view of low-temperature resistance of CuIr_2S_4 under pressures ranging from 18.1-111.8 GPa (D) and 122.2-224 GPa (E). At 111.8 GPa, a new superconducting phase emerges (marked with green arrow) and is enhanced with increasing pressure. The criterion for determining the superconducting transition temperature (T_c) is shown in the figures with black crosswire.

bic to a triclinic structure from the metallic to the insulator phase^{6,19}, seemingly impeding metallic behavior and superconductivity. In comparison, the related compounds CuRh_2S_4 and CuRh_2Se_4 , while showing slight lattice shrinkage and expansion to $a = 9.787 \text{ \AA}$ and $a = 10.269 \text{ \AA}$, respectively¹³, do not exhibit MIT and crystal structure phase transitions, yet they support superconductivity^{13,20}. Intriguingly, superconductivity is also present in the charge density wave (CDW) material CuIr_2Te_4 , which has a trigonal structure²¹. These examples underscore the significant influence of geometric structure on the properties of AB_2X_4 spinel compounds. Notably, the suppression of MIT and the subsequent emergence of superconductivity in Zn-doped CuIr_2S_4 reveal a complex relationship between these phenomena, where increasing Zn content not only suppresses MIT but also induces superconductivity, with transition temperatures of 2.8 K and 2.2 K observed for Zn contents of $x = 0.3$ and $x = 0.5$, respectively²². High pressure has been demonstrated to be a potent means of modifying such traits, and in some instances, it has even triggered transitions from insulating states to metallic and superconducting phases²³⁻²⁵. This raises a fundamental question: can extreme pressure be employed to manipulate CuIr_2S_4 's lattice configuration and unlock its hidden potential for high-temperature superconductivity?

Our work presents a paradigm shift in spinel superconductivity by harnessing the transformative power of high pressure to reveal the extraordinary metamorphosis of CuIr_2S_4 . We employ a combination of high-pressure transport measurements, synchrotron X-ray diffraction, and spectroscopy techniques up to 224 GPa. Under high pressure, CuIr_2S_4 not only suppresses its frustrating lattice distortion but also undergoes a cascade of transformations, culminating in the emergence of not one, but two distinct superconducting phases. The first phase appears at a noteworthy T_c of 3.8 K, progressively ascending with pressure to reach a record-shattering 18.2 K at 133.3 GPa – an achievement exceeding prior benchmarks for both spinel and iridium-based superconductors. Further surprises unfold at higher pressures, where a second, unexpected superconducting phase materializes with a distinct T_c of 2.2 K. This observation indicates the complex unconventional pairing mechanisms in this system.

Our discovery transcends the quest for record-breaking T_c in spinels. It redefines the performance boundaries of spinel materials and illuminates the profound potential concealed within seemingly ordinary compounds.

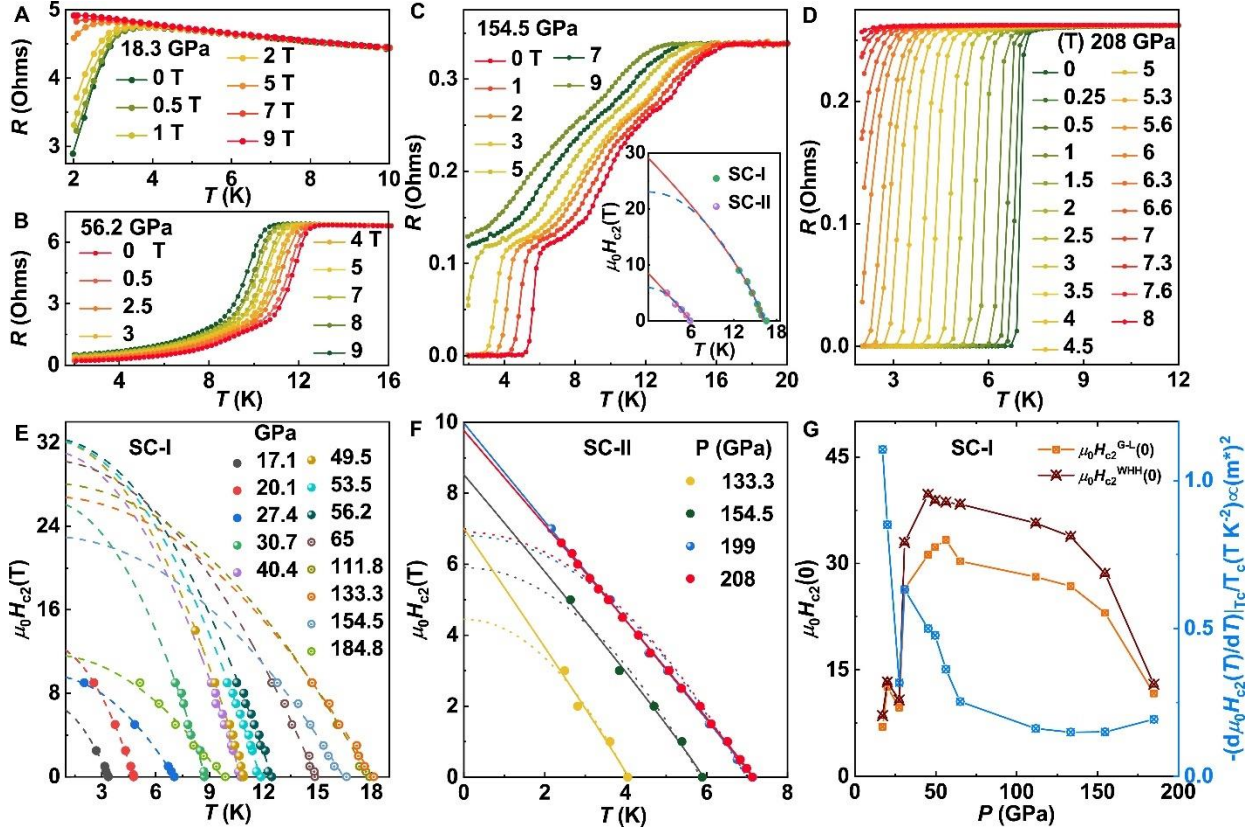


Figure 2. Evolution of superconducting transition as function of magnetic fields in CuIr_2S_4 . (A and B) The temperature dependence of resistivity under different magnetic fields at 18.3 (A) and 56.2 (B), respectively. (C and D) The temperature dependence of resistivity under different magnetic fields at 154.5 (C) and 208 GPa (D), respectively. Inset of (C) show the best fits of T_c vs H employing the G-L formula, solid line using formula (1) and dotted line using formula (2). (E) show the best fits of T_c vs H employing the G-L formula (1). (F) show the best fits of T_c vs H employing the G-L formula, solid line using formula (1) and dotted line using formula (2). (G) Pressure dependence of the zero temperature upper critical field $\mu_0 H_{c2}(0)$ obtained from the G-L fitting and the WHH model, and the normalized slope $-(1/T_c)[d\mu_0 H_{c2}(T)/dT]_{T_c}$.

By unlocking the secrets of CuIr_2S_4 's pressure-induced transformation, we gain invaluable knowledge for shaping the future of quantum materials, paving the way for the design of materials with exotic properties and groundbreaking functionalities.

RESULTS AND DISCUSSION

At ambient pressure, the temperature-dependent resistance measurements ($R(T)$) indicate that CuIr_2S_4 undergoes an MIT during cooling (as shown in Figure S2a), consistent with the previous reports^{19,26}. We conducted high-pressure electrical resistance measurements on CuIr_2S_4 over four runs, using several different culet sizes. Figure 1 illustrates the evolution of the resistance as a function of temperature in a single crystal of CuIr_2S_4 at various pressures, ranging from 1.8 to 224 GPa. With increasing pressure, the MIT critical temperature (T_M) shifts to higher temperatures, and the metallic state is suppressed below 300 K and 4.1 GPa, as shown in Figure 1B, aligning with earlier research²⁷. In the pressure range of 4.1 to 16.8 GPa, $R(T)$ displays insulating behavior with negative temperature coefficients of resistance. Remarkably, at 18.1 GPa, a superconducting state (referred to as SC-I) emerges, characterized by a distinct drop near $T_c = 3.8$ K, as illustrated in Figure 1D, resembling strange metal or granular superconductivity. Here, T_c is defined as the onset temperature

where the drop in resistance is observed. Due to zero resistance appearing at temperatures below our measurement limit (~ 2 K), we could not observe zero resistance until reaching 122.2 GPa, as evidenced in Figure 1E. It is clearly seen that the evolution of T_c under increasing pressure is non-monotonic: initially, T_c rapidly increases from 18.1 to 78.8 GPa, then it slows down and peaks at 18.2 K at 133.3 GPa, before decreasing monotonically with further pressure increase, as demonstrated in Figure 1D and Figure S2b. However, the behavior of the superconducting state in CuRh_2S_4 under pressure differs significantly; it disappears abruptly around a critical pressure of 5.6 GPa and transitions to an insulator¹³. Surprisingly, at 111.8 GPa, a second superconducting phase (SC-II) is observed, demonstrated by a resistance drop at approximately 2.2 K, marked by a green down-pointing arrow in Figure 1E. This resistance drop becomes more pronounced with additional compression, ultimately reaching zero resistance at 122.2 GPa. Notably, this two-step-like transition is reminiscent of phenomena observed in $\text{Bi}_2\text{Sr}_2\text{CaCu}_2\text{O}_{8+\delta}$ ²⁸ and ZrTe_5 ²⁹.

The pressure- T_c phase diagram reveals that two superconducting phases are emergent after the MIT has been suppressed by pressure in CuIr_2S_4 , as depicted in Figure S2b. SC-I spans a broad pressure range from 18.1 to 184.8 GPa, while SC-II exists at pressures ranging from 111.8 to

224 GPa. It is clear that the evolution of T_c^{SC-I} as a function of pressure produces a dome-shaped superconducting regime in the high-pressure phase diagram, reflecting intricate interactions and possible structural instability²⁹⁻³⁰. There is a slight discrepancy observed between different experimental runs in the SC-I state, which is reasonable considering variations in culet size, sample size and pressure calibration in each run. The behavior of T_c^{SC-II} with pressures displays a different trend from that of T_c^{SC-I} . It first increases linearly to 6 K with a slope of 0.081 K/GPa up to 154.5 GPa, starting from 2.6 K at around 111.8 GPa, then ascends with a smaller slope of 0.017 K/GPa to 7.5 K at 224 GPa. These results suggest that the lower-temperature resistance drop is associated with a new superconducting state, indicating the coexistence of two superconducting phases in the sample. Remarkably, CuIr_2S_4 now holds the record for the highest superconducting transition temperature (18.2K) among both spinel and iridium-based superconductors, surpassing the previous records of 13.7 K in spinel LiTi_2O_4 ¹⁵ and 10.5 K in iridium compound $\text{Nb}_5\text{Ir}_3\text{O}$ ³¹⁻³².

To further characterize the superconducting properties of the single crystals of CuIr_2S_4 under pressure, we have examined the effect of magnetic fields and electrical current on resistance at several representative pressures of each run, as shown in Figure 2 and Figure S3-5. Figures 2A and 2B illustrate the $R(T)$ curves under varying magnetic fields at pressures of 18.3 GPa and 56.2 GPa, respectively. At these pressures, only the SC-I was observed. The onset T_c reduces gradually with increased magnetic field strength. Figure 2C reveals that the $R(T)$ curves under various magnetic fields bifurcate into two distinct segments at 154.5 GPa, signifying the coexistence of SC-I and SC-II. SC-II is more sensitive to the magnetic field compared to SC-I. The onset T_c^{SC-II} cannot be identified above 5 T, where superconductivity is dominated by SC-I. Figure 2D illustrates the $R(T)$ curves under different magnetic fields at a pressure of 208 GPa with the only existence of SC-II.

Figure 2E provides details on how we computed the zero-temperature upper critical field ($\mu_0 H_{c2(0)}$) values at specific pressures for SC-I. We applied the Ginzburg-Landau (G-L) formula³³,

$$\mu_0 H_{c2}(T) = \mu_0 H_{c2}(0) \left[1 - \left(\frac{T}{T_c} \right)^2 \right] \quad (1)$$

to fit the $\mu_0 H_{c2(0)}-T$ plots, where T/T_c denotes the reduced temperature. However, in the SC-II region, due to a significant discrepancy between the fitting results using Equation (1) and experimental data (dashed lines Figure 2F), we approximated the $\mu_0 H_{c2(0)}$ value for SC-II using the empirical G-L expression³⁴,

$$\mu_0 H_{c2}(T) = \mu_0 H_{c2}(0) \left(\frac{1-t^2}{1+t^2} \right) \quad (2)$$

where $t = T/T_c$. As a result, at a pressure of 154.5 GPa, the $\mu_0 H_{c2(0)}$ values were estimated at 23.0 T for SC-I and 7.3 T for SC-II, as shown inset of Figure 2C. This substantial difference in the upper critical fields $\mu_0 H_{c2(0)}$ implies distinct properties for SC-I and SC-II.

The value of $\mu_0 H_{c2}(0)$ in the SC-II state exhibits a monotonic evolution with pressure, similar to the monotonic enhancement of $T_c^{SC-II}(P)$ (as depicted in Figure 2F). In contrast, in the SC-I state, the evolution of $\mu_0 H_{c2}(0)$ as a function of pressure is somewhat more complicated. As illustrated in Figure 2G, the obtained value of $\mu_0 H_{c2SC-I}^{G-L}(0)$ initially increases from ~ 7 T at 18.1 GPa to 12.6 T at 20.1 GPa, with a slope of around ~ 2.8 T/GPa. It then decreases to ~ 9.7 T at 27.5 GPa with a slope of ~ -0.4 T/GPa. Upon further compression, the value of $\mu_0 H_{c2SC-I}^{G-L}(0)$ begins to increase rapidly again, reaching 26.4 T at 30.7 GPa with a larger slope of 5.2 T/GPa. Above 30.7 GPa, it continues to rise nearly linearly to ~ 33.3 T with a smaller slope of 0.27 T/GPa, up to 56.2 GPa. With additional compression, the value of $\mu_0 H_{c2SC-I}^{G-L}(0)$ slowly declines to 28.1 T at 111.8 GPa and then decreases rapidly to 11.7 T at 184 GPa, which may be correlated with the suppression of the SC-I superconducting state. Given the uncertainty in obtaining the $\mu_0 H_{c2(0)}$ from the above G-L fitting, we also estimated the $\mu_0 H_{c2(0)}$ using the Werthamer-Helfand-Hohenberg (WHH) formula³⁵,

$$\mu_0 H_{c2}^{WHH}(0) = -0.69 \times T_c \left| \frac{dH_{c2}(T)}{dT} \right|_{T_c} \quad (3)$$

based on the initial slope near T_c . The obtained values, depicted in Figure 2G, are somewhat larger than those from G-L fitting but follow a similar trend under compression. According to the single-band model, the initial slope is related to the Fermi-velocity v_F^{-2} and the effective mass m^* of charge carriers via the relationship³⁶⁻³⁷:

$$-(1/T_c) \left[\frac{d\mu_0 H_{c2}(T)}{dT} \right]_{T_c} \propto v_F^{-2} \propto m^* \quad (4)$$

We further extract the normalized slope $-(1/T_c) \left[\frac{d\mu_0 H_{c2}(T)}{dT} \right]_{T_c}$, which decreases from ~ 1.10 T/K² at 18.1 GPa to about 0.19 T/K² at 184.8 GPa, as shown in Figure 2G. Such a pressure-induced reduction of the effective mass m^* or the electron correlations should correlate with the expansion of bandwidth under high pressures³⁴. An abrupt increase around 27 GPa might be associated with the structural transition, as detailed in the following section.

It is interesting to note that we observe the emergence of a distinct phase near the SC-I state, revealed by spontaneous in-plane anisotropy in resistance. As shown in the inset Figure 3A, the measurements were carried out in a van der Pauw geometry, allowing us to switch the current and voltage leads for measuring current along the V_{\uparrow} (black arrow) crystal axis and perpendicular to the V_{\uparrow} direction. At 18.1 GPa, the resistance of the sample displays an insulator behavior above T_c^{SC-I} for current perpendicular to the V_{\uparrow} crystal axis, hereafter referred to as $R_{\perp}(T)$ just for convenience, whereas it shows metallic characteristics for current along V_{\uparrow} direction, which

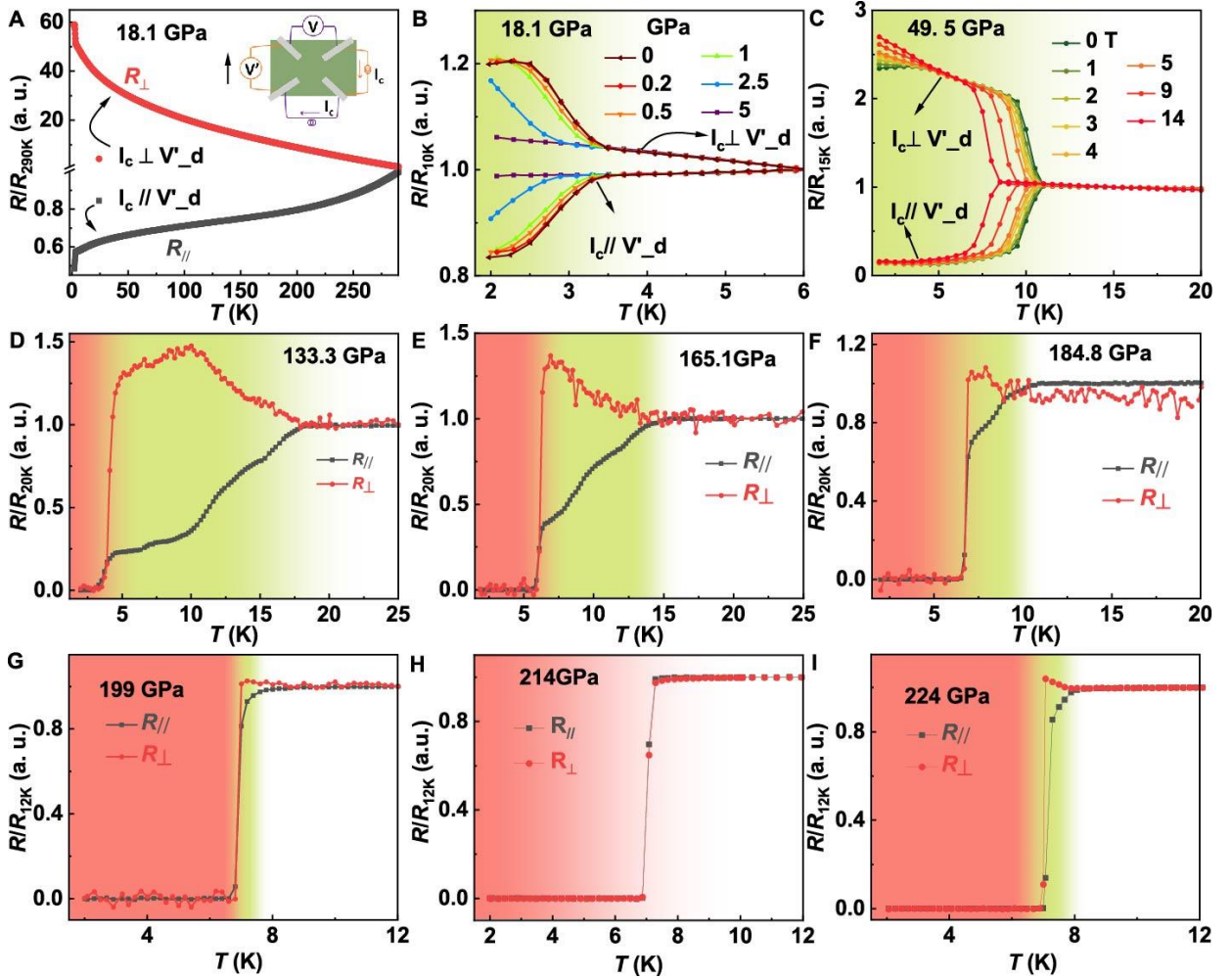


Figure 3. $R_{//}$ and R_{\perp} as a function of temperature in CuIr_2S_4 under varying pressures. (A) $R_{//}(T)$ and $R_{\perp}(T)$ measured at pressures of 18.1 GPa. Inset of (A) shows the integration of electrodes for concurrent measurements of $R_{//}(T)$ and $R_{\perp}(T)$. (B and C) Magnetic field dependence of superconducting temperatures measured along both electric current directions at 18.1 GPa (B) and 49.5 GPa (C). (D and I) $R_{//}(T)$ and $R_{\perp}(T)$ measured at pressures of 133.3 GPa (D), 165.1 GPa (E), 184.8 GPa (F), 199 GPa (G), 214 GPa (H) and 224 GPa (I). Pink zones mean the zero resistance superconducting state, and the green zones represent the “stripe” phase.

named $R_{//}(T)$. As the temperature drops below T_c^{SC-I} , about 3.3 K, $R_{\perp}(T)$ suddenly enhances by almost 20 %, while $R_{//}(T)$ decreases by over 20 %. The appearance of this anisotropy in our sample indicates the emergence of a manifest phase that breaks rotational symmetry on macroscopic length scales³⁸⁻³⁹. The observed anisotropy persists over a broad temperature range, from 3.3 K down to about 2 K (equipment limits), as illustrated with a green background in Figure 3B. It is important to note that while the van der Pauw method can amplify transport anisotropy, the qualitative features reported here are likely to be unaffected⁴⁰. A similar anisotropic superconductivity was also observed in 2D granular superconductors⁴¹, the bulk superconductor $\text{Bi}_2\text{Sr}_2\text{CaCu}_2\text{O}_{8+\delta}$ ²⁸ and at the $\text{KTaO}_3(111)$ interfaces³⁹.

To understand the peculiar nature of the anisotropic superconductivity in the SC-I state, we performed the magnetic field experiments perpendicular to the up-plane of the sample, and measured the resistance $R_{\perp}(T)$ and $R_{//}(T)$, as shown in Figures 3B and 3C. With an increasing mag-

netic field and as temperature drops below T_c^{SC-I} , $R_{\perp}(T)$ decreases, exhibiting a negative magnetoresistance (MR) character, while in contrary, $R_{//}(T)$ increases, showing a positive MR character (see FigureS6). As the magnetic field is increased further above $\mu_0 H_{c2}(0)$, the resistance in both directions transitions to the normal state (indicated by the white background in the figures), and the MR anisotropy disappears, similar to a 'stripe' phase being driven into the normal state^{39,42}. This in-plane anisotropic feature persists in the SC-I state until the onset of the SC-II phase, where both $R_{\perp}(T)$ and $R_{//}(T)$ rapidly drop to zero at T_c^{SC-II} , resulting in a 3D bulk superconducting state, as illustrated by the pink background in Figures 3D-I. The distinctly anisotropic behavior of the SC-I state is gradually suppressed when the pressure increases above 133.3 GPa and vanishes with pressure higher than 199 GPa, as seen in Figure 3H. Interestingly, the anisotropic behavior reemerges at pressures higher than 224 GPa, as shown in

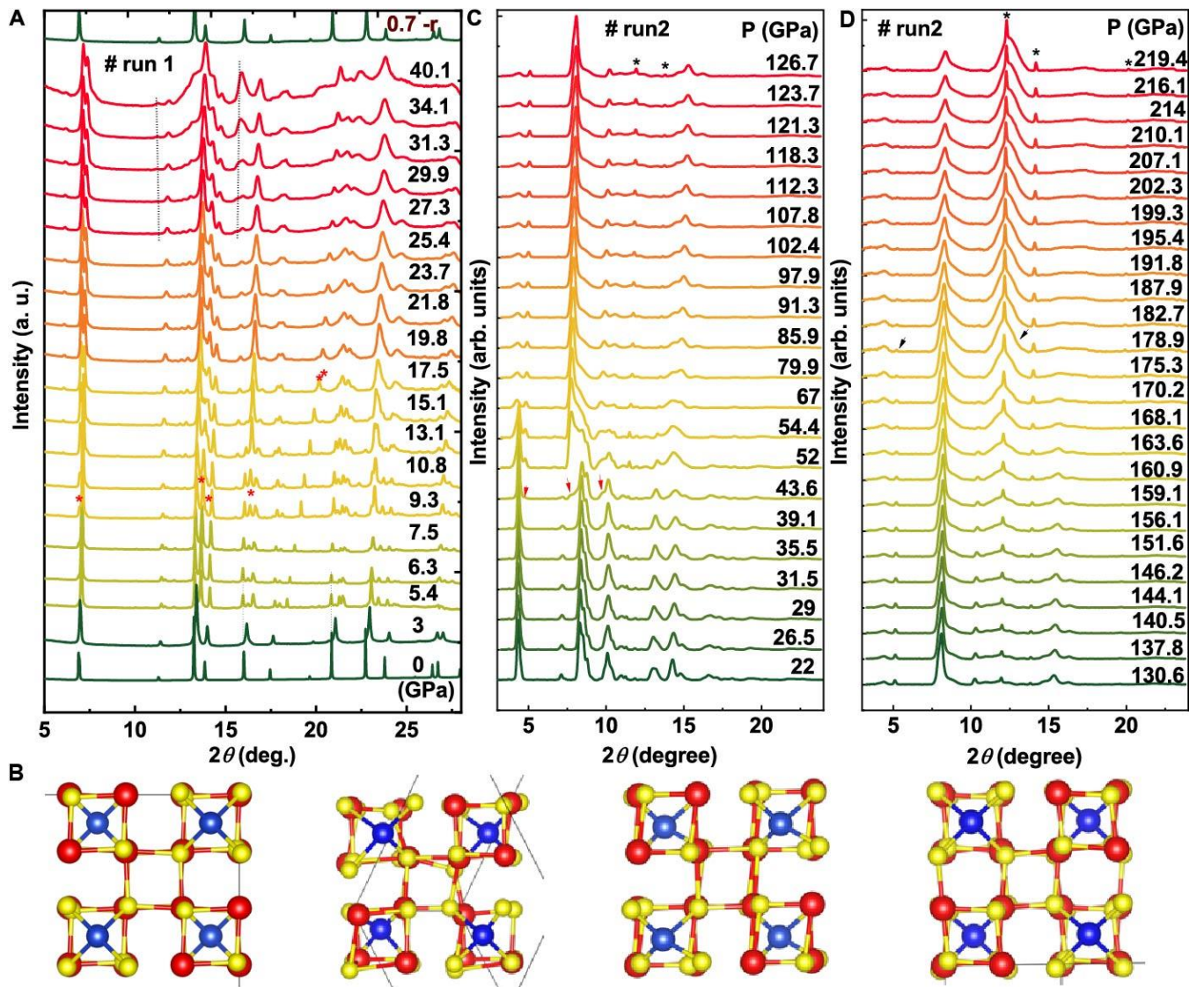


Figure 4. Pressure-induced structural phase transition in CuIr_2S_4 . (A) XRD patterns measured in CuIr_2S_4 under high pressure up to 40.1 GPa with an incident wavelength $\lambda = 0.68883 \text{ \AA}$. Stars and dotted-line indicate the present of new peaks. (B) Pressure-induced transformation of crystalline from metallic cubic phase to triclinic insulator phase and finally orthorhombic superconductive phase. (C and D) Synchrotron XRD patterns with subtracted background of CuIr_2S_4 at various pressures up to 219.4 GPa an incident wavelength $\lambda = 0.434 \text{ \AA}$. Black stars here present the Au peaks for pressure calibration.

Figure S1 and Figure S7.

To further explore the crystal structures of the SC-I and SC-II phase, high-pressure powder X-ray diffraction (PXRD) experiments on CuIr_2S_4 were conducted up to 219.4 GPa at room temperature, as illustrated in Figure 4. At ambient pressure, the diffraction pattern can be indexed very well with a space group $Fd\bar{3}m$ (see detailed in Table S1-2) as reported in the previous study¹⁰ (named phase I). With increasing pressure, the peaks shift to higher angles, indicating a shrinkage in the lattice parameters. Around 3 GPa, a new insulating phase II emerges, marked by additional XRD peaks and is fully developed at 5.4 GPa. Phase II is characterized by triclinic symmetry of the $P-1$ space group, intricate charge ordering of $\text{Ir}^{3+}\text{-Ir}^{4+}$, and spin dimerization, similar to the low temperature phase I at ambient pressure⁶. Phase III appears at 9.3 GPa, followed by phase IV at 17.5 GPa, representing a structural transition from the triclinic to an orthorhombic phase. This change, revealed by high-

pressure single crystal XRD measurements, likely hosts the SC-I.

The predominant changes in crystal structures under pressure occur within the $[\text{IrS}_6]$ octahedra, as illustrated in Figure 4B, detailed Rietveld refinement of the XRD patterns of CuIr_2S_4 at different phases as shown in Figure S8. From a chemical coordination perspective, the structural units are differentiated with $[\text{IrS}_6]$ framework and $[\text{CuS}_4]$ tetrahedron to examine the structural evolution under pressure, as depicted in Figure S1c. With increasing pressure, the geometrical distortion of $[\text{IrS}_6]$ octahedra escalates rapidly, corresponding to the different crystal structures across various phases. The pressure-induced superconductivity in CuIr_2S_4 , accompanied by structural transitions, sets it apart from numerous other spinel compounds^{12-13, 20, 22}, where superconductivity typically emerges in the cubic phase, suggesting a unique superconducting mechanism in this case. Upon further compression, two distinct

peaks appear around 11.23 and 15.7 degrees, starting at 27.3 GPa. These peaks intensify with continuous compression, indicating a new structural transition (referred to as phase V), which coincides with the increase in $\mu_0 H_{c2(0)}$ illustrated in Figure 2G. Our pressure-dependent Raman measurements, as presented in Figure S9⁴³⁻⁴⁹, validate the structural transformations detected in XRD measurements up to 40 GPa.

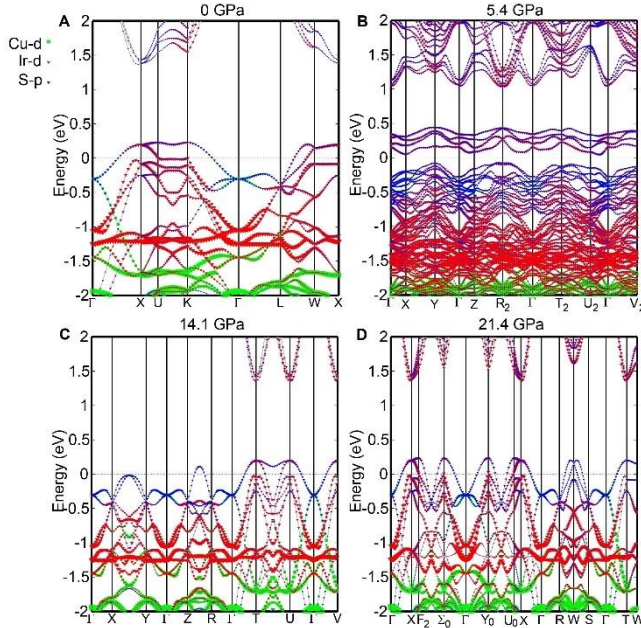


Figure 5. Low-pressure electronic structures of CuIr_2S_4 . (A, B, C and D) Band structure of CuIr_2S_4 obtained by DFT calculations under different pressures at 0 GPa (A), 5.4 GPa (B), 14.1 GPa (C) and 21.4 GPa (D). The orbital characters of bands are represented by the different colors and the projected weights are represented by the sizes.

A new structural phase transition is confirmed by the emergence of three new Bragg peaks at 43.6 GPa (indicated by red arrows in Figure 4C). It completely transforms into a new phase (named phase VI) at around 67 GPa. When pressure exceeds 178.9 GPa (Figure 4D), a new reversible structural phase transition (named phase VII) occurs, characterized by a peak disappearing around 5.2 degrees and a broad peak emerging around 12.6 degrees. The phase VII remains stable with pressure up to 219.4 GPa, the highest pressure applied in these experiments. It is interesting to note that the pressure at which phase VII occurs approximates the pressure at which the SC-I submerges in transport results. We did not find any newly emerged peaks from high-pressure phases of sulfur⁵⁰⁻⁵¹, which suggests that all the structural phase transitions¹³ occur in CuIr_2S_4 , and the original superconductivity originates from CuIr_2S_4 . It is noteworthy that the superconductivity observed in the related compounds CuRh_2S_4 , CuRh_2Se_4 ^{13,20}, and doped $\text{Cu}_{1-x}\text{Zn}_x\text{Ir}_2\text{S}_4$ ²² distinctly stands out, as it occurs within their cubic structure without any structural phase transitions.

To elucidate the physics underlying the observed superconductivity in CuIr_2S_4 under pressure, we utilized first-principles calculations based on density functional theory (DFT). We investigated the electronic structure of CuIr_2S_4

across the first four phases. Figure 5 and Figure S10 reveal the dominance of Ir-5d states at the Fermi level, with moderate hybridization from S-3p states, while Cu-3d content is almost negligible. At ambient pressure, CuIr_2S_4 shows metallic ground states, consistent with previous findings⁵². Under compression, distinct transitions occur: a 0.2–0.3 eV energy gap emerges at 5.4 GPa in the triclinic structure. At 14.1 GPa (phase III) and 21.4 GPa (phase IV), CuIr_2S_4 reverts to metallic ground states. This indicates that structural transitions are pivotal in the emergence of superconductivity. Moreover, in the phase IV, where superconductivity first emerges, the hybridization between Ir-5d orbitals and S-3p orbitals near the Fermi level becomes stronger, indicating that the sizable *d-p* coupling may play an important role in metallization and superconductivity.

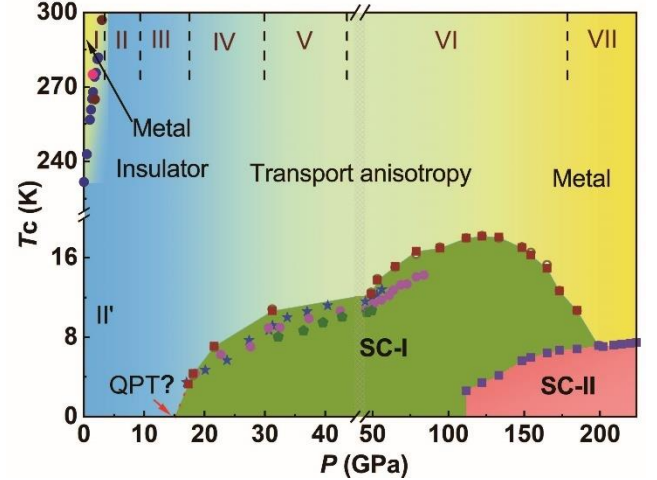


Figure 6. Pressure–temperature phase diagram of CuIr_2S_4 . Black dashed lines denote the phase boundaries of structures under pressure at room temperature. II' is ambient pressure low temperature insulating phase mentioned in Ref.⁶. Gray dense pattern represents the break region of pressure. Different symbols represent the T_{MIT} , and T_c of SC-I and SC-II measured in different runs.

All characteristic parameters from our experiments are encapsulated in the pressure–temperature phase diagram in Figure 6. With increasing compression, the T_M rises, disappearing around 3 GPa as the system transitions to insulating phase II. A gradual weakening in insulation during phase III leads to an emergent superconducting phase (SC-I), hinting at a possible quantum critical point near 18 GPa.

We discerned extremely anisotropic magnetoresistance (MR) in phase V of SC-I (as shown in Figure S11), which is tied to the magnetic configuration of CuIr_2S_4 , and clear quantum oscillations (see Figure S11(a)) that vanish at 30 GPa. Future studies are necessary to understand the magnetic properties near the quantum phase transition (QPT) and the evolution of superconductivity.

As compression extends beyond 18 GPa, T_c peaks at 18.3 K at 133.3 GPa before declining, with SC-I disappearing at 199 GPa. SC-II appears exclusively above 111.1 GPa, growing monotonically to 224 GPa and reaching a T_c of 7.2 K. Pressure-induced SC-II is identified as a bulk superconductor, distinct from SC-I. The resistance drop near 3.0 K at 18 GPa may be attributed to factors like 2D superconductivity, with the notably anisotropic behavior of SC-I being compa-

rable to bismuth-based cuprate superconductors²⁸. Hence, SC-I is possibly linked to unconventional superconductivity. However, the specific plane associated with CuIr_2S_4 's 2D superconducting state remains unverified, and this study's observation of a pressure-induced crossover from 2D to 3D bulk states is unprecedented among compressed bulk iridate superconductors.

CONCLUSIONS

In summary, we have explored CuIr_2S_4 's high-pressure structural evolution and electronic properties through electrical resistance, synchrotron XRD, and Raman measurements. We successfully initiated superconductivity in CuIr_2S_4 using high pressure, achieving a maximum T_c of 18.2 K at about 133.3 GPa—setting a new standard for spinels and iridium-based compounds. The T_c -P phase diagram reveals a dome-like superconducting phase, suggesting potential structural instability at extreme pressures. A novel bulk superconducting state, SC-II, starts around 111.1 GPa with an initial T_c of 2.2 K, rising to 7.2 K near 224 GPa. Our findings also highlight metal-insulator transitions, quantum oscillations in MR, and superconductivity in CuIr_2S_4 , enriching the fascinating physics of spinels. This research provides valuable insights into iridium superconductors and invites further investigations, including theoretical explorations and advanced high-pressure experiments to unravel the pairing mechanism in this intriguing system.

MATERIALS AND METHODS

Single crystal growth and characterization. The high-quality single crystals of CuIr_2S_4 used in our measurements were grown by a flux method and the structural parameters at ambient condition were obtained by single-crystal X ray diffraction. Single crystals of CuIr_2S_4 were grown from bismuth (Bi) solution and the detailed can be found elsewhere⁵³. CuIr_2S_4 powders were first synthesized by a solid-state reaction method. To synthesize CuIr_2S_4 powders, high purity powders of Cu (99.99%), Ir (99.99%) and S (99.999%) powders as starting materials were sealed into an evacuated quartz tube and sintered at 850 °C for 3 d. Then, the prepared CuIr_2S_4 powders and high purity Bi (99.99%) were mixed together with the ratio of CuIr_2S_4 : Bi = 1: 100, and sealed into an evacuated quartz tube. The mixture was first heated to 1100 °C for 50 h and then slowly cooled down to 550 °C at the rate of 2 °C/h to grow the single crystals. Large crystals with sizes of several millimeters were obtained from the Bi flux by centrifuging at 550 °C. The samples were characterized by single-crystal XRD measurements using a Bruker D8 Quest diffractometer equipped with Mo $K\alpha$ radiation. The data reduction, structure solution, and refinement were carried out with program APEX3⁵⁴⁻⁵⁵. The refinement details can be found in the SM of Tables S1, in agreement with previous studies^{10,53}.

High-pressure synchrotron PXRD measurements. The high-pressure synchrotron PXRD measurements up to 40.1 GPa of run 1 were performed at room temperature at the beamline BL12B2 of Spring-8 with a 18 keV ($\lambda = 0.68883$ Å) beam to verify the phases and volume of CuIr_2S_4 . A symmetric DAC was used to generate pressure with a pair of 400 μm culet size anvils. A T301 stainless steel gasket prepressed to 40 μm thickness with a 150 μm

sample chamber was used. An appropriate amount of CuIr_2S_4 powders grinded from CuIr_2S_4 single crystal were loaded into the pressure chamber with Ne gas as a pressure medium. The pressure was determined via monitoring the fluorescence of the ruby near the sample. The sample-to-detector distance and other parameters of the detector were calibrated using the CeO_2 standard. The diffraction images were integrated using the Dioptas program⁵⁶ and structure refinements were conducted by using the Rietveld method in the General Structure Analysis System (GSAS)⁵⁷ program. The ultra-high pressure synchrotron PXRD experiments up to 219 GPa of run2 were performed at beamline 13BM-C of GeoSoilEnviroCARS (GSECARS) at Advanced Photon Source (APS), Argonne National Laboratory (ANL). The wavelength of the monochromatic X-ray beam is 0.434 Å. The diffraction patterns were collected by the MarCCD detector and integrated using the Dioptas software⁵⁶.

High-pressure X-ray single-crystal diffraction. The high-pressure X-ray single-crystal diffraction measurements were performed on CuIr_2S_4 single crystal up to 34.1 GPa at room temperature using a Bruker D8 Quest diffractometer equipped with Mo $K\alpha$ radiation. Data were collected with a Sc-type DAC. Neon was used as the pressure transmitting medium. The data reduction, structure solution, and refinement were carried out with program APEX3⁵⁴⁻⁵⁵.

Raman spectroscopy measurements. Raman spectra were collected in a backscattering geometry using a Renishaw Raman microscope. A laser excitation wavelength of 532 nm was applied to obtain the sample's Raman spectra. The laser power was limited to less than 1.8 mW to avoid the sample overheating. A single crystal CuIr_2S_4 was chosen to measure, and all Raman measurements were performed on the same surface. Neon was used as the pressure transmitting medium and the ruby fluorescence was used to calibrate the pressure.

High-pressure transport measurements. Symmetric type anvil cells composed of BeCu with various culets size from 100 μm to 300 μm were used for high-pressure transport measurements. The Re gasket was pre-indented to 20 μm and then drilled with a hole of 290 μm in diameter at the center of imprint. Fine insulating cubic boron nitride (cBN) powders mixed with epoxy were filled into the hole and further pressed with anvils to form a solid layer of ~ 15 μm in thickness. A hole of 60 μm in diameter was drilled at the center of the solid cBN layer to serve as the sample chamber. NaCl was used as a pressure transmitting medium. The four-probe method was applied for all high-pressure transport measurements. The Pt foils with a thickness of 3 μm were deposited on the surface of the culet as the inner electrodes. Copper wire was attached to the Pt foils to serve as the outside electrodes. For each measurement cycle, the pressure was calibrated by using the shift of ruby fluorescence and diamond Raman at room temperature. The transport measurements were performed on a Quantum Design instrument physical property measurement system (PPMS) with a magnetic field up to 9 T and temperature from 2 to 300 K. The higher magnetic field from 9 to 14 T measurements were carried out in a

homemade multifunctional measurement system (1.5–300 K, PHYSIKE Inc.; 0–14 T, Cryomagnetics Inc.).

First-principles calculations. Our density functional theory (DFT) calculation is performed by Vienna ab initio simulation package (VASP) code⁵⁸ with the projector augmented wave (PAW) method⁵⁹. The Perdew-Burke-Ernzerhof (PBE)⁶⁰ exchange-correlation functional is used in our calculation. The kinetic energy cutoff is set to be 600 eV for the expanding the wave functions into a plane-wave basis and the energy convergence criterion is 10^{-6} eV. The Monkhorst-Pack k-mesh is set as $8 \times 8 \times 8/6 \times 8 \times 6/8 \times 8 \times 8/8 \times 8 \times 8$ for CuIr_2S_4 under 0.5, 4, 14.1 and 21.4 GPa. All of the crystal structures are fully relaxed while forces are minimized to less than 0.005 eV/Å.

ASSOCIATED CONTENT

Supporting Information.

Additional experimental data and calculation results including detailed Rietveld refinement of the XRD patterns of CuIr_2S_4 at different pressures and magnetic fields, temperature dependence of the electrical resistance at representative pressures, in situ high-pressure Raman spectra, total DOS of CuIr_2S_4 at different pressures. This material is available free of charge via the Internet at <http://pubs.acs.org>.

AUTHOR INFORMATION

Corresponding Author

* To whom correspondence should be addressed. E-mail: juan_chen@fas.harvard.edu, jphu@iphy.ac.cn, yang.ding@hpstar.ac.cn

Present Addresses

†Department of Physics, Harvard University, Cambridge, Massachusetts 02138, USA

Author Contributions

B.J.C. and Y.D. conceived the idea and designed the experiments. B.J.C. were responsible for high-pressure in site electronic transport experiments with the assistance of W.D., D.W., M.L.J., Y.Z., J.B.Z., and Y.W.L.; B.J.C. performed high pressure synchrotron XRD and single crystal XRD measurements with the assistance of H.I., Y.-F.L., D.Z.Z. and D.W.; B.J.C. performed the high pressure Raman experiments with the assistance of L.X.Y.; H.X., B.J.C., and D.W. performed sample synthesis. B.J.C. analyzed the experimental data; Y.H.G. performed the electronic band calculations. B.J.C. and Y.D. wrote the manuscript. All authors have interpreted the findings, commented on the paper, and approved the final version.

Funding Sources

Any funds used to support the research of the manuscript should be placed here (per journal style).

Notes

The authors declare no competing financial interest.

ACKNOWLEDGMENT

This work was supported by the National Natural Science Foundation of China (NSFC) grant No. 11874075 and 11934017, Science Challenge Project No. TZ2016001, and National Key Research and Development Program of China 2018YFA0305703, 2022YFA1403901 and 2021YFA1400300. The XRD measurements at SPring-8 were carried out under

the proposals of 2019A4132. The XRD experiments performed at GeoSoilEnviroCARS (The University of Chicago, Sector 13), Advanced Photon Source (APS), Argonne National Laboratory is supported by the National Science Foundation – Earth Sciences (EAR – 1634415), this research used resources of the Advanced Photon Source, a U.S. Department of Energy (DOE) Office of Science User Facility operated for the DOE Office of Science by Argonne National Laboratory under Contract No. DE-AC02-06CH11357. J.P. Hu acknowledges supports from New Cornerstone Investigator Program and H.-K. Mao acknowledges supports from the National Natural Science Foundation of China Grant No. U1530402 and U1930401. B.J. Chen thanks Dr. X.X.Wu, Dr. J. Song, Dr. Z.Deng, Dr. S.J.Zhang and Dr. S.M.Feng for the help during transport experiments and valuable discussions.

REFERENCES

1. Patoux, S.; Daniel, L.; Bourbon, C.; Lignier, H.; Pagano, C.; Le Cras, F.; Jouanneau, S.; Martinet, S., High voltage spinel oxides for Li-ion batteries: From the material research to the application. *J. Power Sources* **2009**, *189* (1), 344-352.
2. Vestal, C. R.; Zhang, Z. J., Synthesis and magnetic characterization of Mn and Co spinel ferrite-silica nanoparticles with tunable magnetic core. *Nano. Lett.* **2003**, *3* (12), 1739-1743.
3. Liu, C.; Zou, B.; Rondinone, A. J.; Zhang, Z. J., Chemical control of superparamagnetic properties of magnesium and cobalt spinel ferrite nanoparticles through atomic level magnetic couplings. *J. Am. Chem. Soc.* **2000**, *122* (26), 6263-6267.
4. Senn, M. S.; Wright, J. P.; Atfield, J. P., Charge order and three-site distortions in the Verwey structure of magnetite. *Nature* **2011**, *481* (7380), 173-6.
5. S.-H. Lee; C. Broholm; W. Ratcliff; G. Gasparovic; Q. Huang; T. H. Kim; Cheong, S.-W., Emergent excitations in a geometrically frustrated magnet. *Nature* **2002**, *418*, 856–858.
6. Radaelli, P. G.; Horibe, Y.; Gutmann, M. J.; Ishibashi, H.; Chen, C. H.; Ibberson, R. M.; Koyama, Y.; Hor, Y. S.; Kiryukhin, V.; and Cheong, S. W., Formation of isomorphous Ir^{3+} and Ir^{4+} octamers and spin dimerization in the spinel CuIr_2S_4 . *Nature* **2002**, *416*, 155-158.
7. Jin, K.; He, G.; Zhang, X.; Maruyama, S.; Yasui, S.; Suchocki, R.; Shin, J.; Jiang, Y.; Yu, H. S.; Yuan, J.; Shan, L.; Kusmartsev, F. V.; Greene, R. L.; Takeuchi, I., Anomalous magnetoresistance in the spinel superconductor LiTi_2O_4 . *Nat. Commun.* **2015**, *6* (1), 7183.
8. Verwey, E., Electronic conduction of magnetite (Fe_3O_4) and its transition point at low temperatures. *Nature* **1939**, *144* (3642), 327-328.
9. Urano, C.; Nohara, M.; Kondo, S.; Sakai, F.; Takagi, H.; Shiraki, T.; Okubo, T., LiV_2O_4 spinel as a heavy-mass Fermi liquid: Anomalous transport and role of geometrical frustration. *Phys. Rev. Lett.* **2000**, *85* (5), 1052.
10. Furubayashi, T.; Matsumoto, T.; Hagino, T.; Nagata, S., Structural and Magnetic Studies of Metal-Insulator Transition in Thiospinel CuIr_2S_4 . *J. Phys. Soc. Jpn.* **1994**, *63* (9), 3333-3339.
11. Ma, L.; Han, H.; Liu, W.; Yang, K.; Zhu, Y.; Zhang, C.; Pi, L.; Liu, D.; Zhang, L.; Zhang, Y., Opposite pressure effects in the orbitally-induced Peierls phase transition systems CuIr_2S_4 and MgTi_2O_4 . *Dalton Trans* **2017**, *46* (20), 6708-6714.
12. Moshopoulou, E. G., Superconductivity in the Spinel Compound LiTi_2O_4 . *J. Am. Ceram. Soc.* **1999**, *82*, 3317-3320.
13. Ito, M.; Hori, J.; Kurisaki, H.; Okada, H.; Perez Kuroki, A. J.; Ogita, N.; Udagawa, M.; Fujii, H.; Nakamura, F.; Fujita, T.; Suzuki, T., Pressure-induced superconductor-insulator transition in the spinel compound CuRh_2S_4 . *Phys. Rev. Lett.* **2003**, *91* (7), 077001.
14. Hagino, T.; Seki, Y.; Wada, N.; Tsuji, S.; Shirane, T.; Kumagai, K.-i.; Nagata, S., Superconductivity in spinel-type compounds CuRh_2S_4 and CuRh_2Se_4 . *Phys. Rev. B* **1995**, *51* (18), 12673.

15. Johnston, D. C., Superconducting and normal state properties of $\text{Li}_{1-x}\text{Ti}_2-x\text{O}_4$ spinel compounds. I. Preparation, crystallography, superconducting properties, electrical resistivity, dielectric behavior, and magnetic susceptibility. *J. Low Temp. Phys.* **1976**, *25*, 145-175.
16. Radaelli, P. G., Orbital ordering in transition-metal spinels. *New J. Phys.* **2005**, *7*, 53-53.
17. Okada, Y.; Ando, Y.; Shimizu, R.; Minamitani, E.; Shiraki, S.; Watanabe, S.; Hitosugi, T., Scanning tunnelling spectroscopy of superconductivity on surfaces of LiTi_2O_4 (111) thin films. *Nat. Commun.* **2017**, *8* (1), 15975.
18. Ortiz, B. R.; Gomes, L. C.; Morey, J. R.; Winiarski, M.; Bordelon, M.; Mangum, J. S.; Oswald, I. W.; Rodriguez-Rivera, J. A.; Neilson, J. R.; Wilson, S. D., New kagome prototype materials: discovery of KV_3Sb_5 , RbV_3Sb_5 , and CsV_3Sb_5 . *Phys. Rev. Mater.* **2019**, *3* (9), 094407.
19. S. Nagata; T. Hagino; Y. Seki; Bitoh, T., Metal-insulator transition in thiospinel CuIr_2S_4 . *Physica B* **1994**, *194*, 1077.
20. Robbins, M.; Willens, R. H.; Miller, R. C., Superconductivity in the spinels CuRh_2S_4 and CuRh_2Se_4 . *Solid State Commun.* **1967**, *5* (12), 933-934.
21. Dong Yan; Yijie Zeng; Guohua Wang; Yiyuan Liu; Junjie Yin; Tay-Rong Chang; Hsin Lin; Meng Wang; Jie Ma; Shuang Jia; Dao-Xin Yao; Luo, H., CuIr_2Te_4 : a quasi-two-dimensional ternary telluride chalcogenide superconductor *arXiv:1908.05438* **2019**.
22. Suzuki, H.; Furubayashi, T.; Cao, G.; Kitazawa, H.; Kamimura, A.; Hirata, K.; Matsumoto, T., Metal-Insulator Transition and Superconductivity in Spinel-Type System $\text{Cu}_{1-x}\text{Zn}_x\text{Ir}_2\text{S}_4$. *J. Phys. Soc. Jpn.* **1999**, *68* (8), 2495-2497.
23. Chen, B.; Parschke, E. M.; Chen, W. C.; Scoggins, B.; Li, B.; Balasubramanian, M.; Heald, S.; Zhang, J.; Deng, H.; Sereika, R.; Sorb, Y.; Yin, X.; Bi, Y.; Jin, K.; Wu, Q.; Chen, C. C.; Ding, Y.; Mao, H. K., Probing Cerium 4f States across the Volume Collapse Transition by X-ray Raman Scattering. *J. Phys. Chem. Lett.* **2019**, *10* (24), 7890-7897.
24. Mao, H.-K.; Chen, X.-J.; Ding, Y.; Li, B.; Wang, L., Solids, liquids, and gases under high pressure. *Rev. Mod. Phys.* **2018**, *90* (1), 015007.
25. Chen, B.; Tian, M.; Zhang, J.; Li, B.; Xiao, Y.; Chow, P.; Kenney-Benson, C.; Deng, H.; Zhang, J.; Sereika, R.; Yin, X.; Wang, D.; Hong, X.; Jin, C.; Bi, Y.; Liu, H.; Liu, H.; Li, J.; Jin, K.; Wu, Q.; Chang, J.; Ding, Y.; Mao, H. K., Novel Valence Transition in Elemental Metal Europium around 80 GPa. *Phys. Rev. Lett.* **2022**, *129* (1), 016401.
26. Garg, A. B.; Vijayakumar, V.; Godwal, B. K.; Choudhury, A.; Hochheimer, H. D., Reentrant high-conduction state in CuIr_2S_4 under pressure. *Solid State Commun.* **2007**, *142* (7), 369-372.
27. Oomi, G.; Kagayama, T.; Yoshida, I.; Hagino, T.; Nagata, S., Effect of pressure on the metal-insulator transition temperature in thiospinel CuIr_2S_4 . *J. Magn. Magn. Mater.* **1995**, *140*, 157-158.
28. Guo, J.; Zhou, Y.; Huang, C.; Cai, S.; Sheng, Y.; Gu, G.; Yang, C.; Lin, G.; Yang, K.; Li, A.; Wu, Q.; Xiang, T.; Sun, L., Crossover from two-dimensional to three-dimensional superconducting states in bismuth-based cuprate superconductor. *Nat. Phys.* **2019**, *16* (3), 295-300.
29. Pan, X. C.; Chen, X.; Liu, H.; Feng, Y.; Wei, Z.; Zhou, Y.; Chi, Z.; Pi, L.; Yen, F.; Song, F.; Wan, X.; Yang, Z.; Wang, B.; Wang, G.; Zhang, Y., Pressure-driven dome-shaped superconductivity and electronic structural evolution in tungsten ditelluride. *Nat. Commun.* **2015**, *6*, 7805.
30. Zhou, Y.; Wu, J.; Ning, W.; Li, N.; Du, Y.; Chen, X.; Zhang, R.; Chi, Z.; Wang, X.; Zhu, X.; Lu, P.; Ji, C.; Wan, X.; Yang, Z.; Sun, J.; Yang, W.; Tian, M.; Zhang, Y.; Mao, H. K., Pressure-induced superconductivity in a three-dimensional topological material ZrTe_5 . *Proc. Natl. Acad. Sci. U S A* **2016**, *113* (11), 2904-9.
31. Zhang, Y.; Wang, B.; Xiao, Z.; Lu, Y.; Kamiya, T.; Uwatoko, Y.; Kageyama, H.; Hosono, H., Electride and superconductivity behaviors in Mn₅Si₃-type intermetallics. *npj Quantum Mater.* **2017**, *2* (1), 45.
32. Wang, B.; Zhang, Y.; Xu, S.; Ishigaki, K.; Matsubayashi, K.; Cheng, J.-G.; Hosono, H.; Uwatoko, Y., Robust two-gap strong coupling superconductivity associated with low-lying phonon modes in pressurized $\text{Nb}_5\text{Ir}_3\text{O}$ superconductors. *Chin. Phys. B* **2019**, *28* (10).
33. Li, Q.; Zhang, J.; Zheng, Q.; Guo, W.; Cao, J.; Jin, M.; Zhang, X.; Li, N.; Wu, Y.; Ye, X.; Chen, P.; Zhu, J.; Wang, T.; Shi, W.; Wang, F.; Yang, W.; Qin, X., Pressure-Induced Superconductivity in HgTe Single-Crystal Film. *Adv. Sci. (Weinh)* **2022**, *9* (18), e2200590.
34. Wang, N. N.; Yang, M. W.; Yang, Z.; Chen, K. Y.; Zhang, H.; Zhang, Q. H.; Zhu, Z. H.; Uwatoko, Y.; Gu, L.; Dong, X. L.; Sun, J. P.; Jin, K. J.; Cheng, J. G., Pressure-induced monotonic enhancement of T_c to over 30 K in superconducting $\text{Pr}_{0.82}\text{Sr}_{0.18}\text{NiO}_2$ thin films. *Nat. Commun.* **2022**, *13* (1), 4367.
35. Li, Z.; He, X.; Zhang, C.; Wang, X.; Zhang, S.; Jia, Y.; Feng, S.; Lu, K.; Zhao, J.; Zhang, J.; Min, B.; Long, Y.; Yu, R.; Wang, L.; Ye, M.; Zhang, Z.; Prakapenka, V.; Chariton, S.; Ginsberg, P. A.; Bass, J.; Yuan, S.; Liu, H.; Jin, C., Superconductivity above 200 K discovered in superhydrides of calcium. *Nat. Commun.* **2022**, *13* (1).
36. Kogan, V.; Prozorov, R., Orbital upper critical field and its anisotropy of clean one- and two-band superconductors. *Rep. Prog. Phys.* **2012**, *75* (11), 114502.
37. Kaluarachchi, U. S.; Taufour, V.; Böhmer, A. E.; Tanatar, M. A.; Bud'ko, S. L.; Kogan, V. G.; Prozorov, R.; Canfield, P. C., Non-monotonic pressure evolution of the upper critical field in superconducting FeSe . *Phys. Rev. B* **2016**, *93* (6), 064503.
38. Barzykin, V.; Gor'kov, L. P., Inhomogeneous stripe phase revisited for surface superconductivity. *Phys. Rev. Lett.* **2002**, *89* (22), 227002.
39. Liu, C.; Yan, X.; Jin, D.; Ma, Y.; Hsiao, H.W.; Lin, Y.; Bretz-Sullivan, T.M.; Zhou, X.; Pearson, J.; Fisher, B. and Jiang, J.S., Two-dimensional superconductivity and anisotropic transport at KTaO_3 (111) interfaces. *Science* **2021**, *371*(6530), 716-721.
40. Miccoli, I.; Edler, F.; Pfnur, H.; Tegenkamp, C., The 100th anniversary of the four-point probe technique: the role of probe geometries in isotropic and anisotropic systems. *J. Phys. Condens. Matter.* **2015**, *27* (22), 223201.
41. Jaeger, H. M.; Haviland, D. B.; Orr, B. G.; Goldman, A. M., Onset of superconductivity in ultrathin granular metal films. *Phys. Rev. B Condens. Matter.* **1989**, *40* (1), 182-196.
42. Jin, M.; Yu, P.; Fan, C.; Li, Q.; Kong, P.; Shen, Z.; Qin, X.; Chi, Z.; Jin, C.; Liu, G.; Zhong, G.; Xu, G.; Liu, Z.; Zhu, J., Discovery of Dome-Shaped Superconducting Phase and Anisotropic Transport in a van der Waals Layered Candidate NbIrTe_4 under Pressure. *Adv. Sci. (Weinh)* **2021**, *8* (24), e2103250.
43. Zwinscher, J.; Lutz, H., Lattice dynamics of spinel-type chlorides, oxides, sulphides and selenides. *J. Alloys and Compd.* **1995**, *219* (1-2), 103-106.
44. Lutz, H.; Himmrich, J.; Haeuseler, H., Lattice Vibration Spectra. LX. Lattice Dynamical Calculations on Spinel Type MCr_2S_4 (M= Mn, Fe, Cd). *Zeitschrift für Naturforschung A* **1990**, *45* (7), 893-902.
45. Amundsen, B.; Burns, G. R.; Islam, M. S.; Kanoh, H.; Rozière, J., Lattice dynamics and vibrational spectra of lithium manganese oxides: A computer simulation and spectroscopic study. *J. Phys. Chem. B* **1999**, *103* (25), 5175-5180.
46. Popović, Z.; De Marzi, G.; Konstantinović, M.; Cantarero, A.; Dohčević-Mitrović, Z.; Isobe, M.; Ueda, Y., Phonon properties of the spinel oxide MgTi_2O_4 with the $S=1/2$ pyrochlore lattice. *Phys. Rev. B* **2003**, *68* (22), 224302.
47. Lutz, H.; Becker, W.; Müller, B.; Jung, M., Raman single crystal studies of spinel type MCr_2S_4 (M = Mn, Fe, Co, Zn, Cd), MIn_2S_4 (M = Mn, Fe, Co, Ni), $\text{MnCr}_{2-2x}\text{In}_{2x}\text{S}_4$ and $\text{Co}_{1-x}\text{Cd}_x\text{Cr}_2\text{S}_4$. *J. Raman Spectrosc.* **1989**, *20* (2), 99-103.
48. Zhang, L.; Ling, L. S.; Qu, Z.; Tong, W.; Tan, S.; Zhang, Y. H., Study of lattice dynamics in the CuIr_2S_4 system. *Eur. Phys. J. B* **2010**, *77* (1), 83-86.

49. Naseska, M.; Sutar, P.; Vengust, D.; Tsuchiya, S.; Čeh, M.; Mihailovic, D.; Mertelj, T., Orbitally driven insulator-metal transition in CuIr_2S_4 : Temperature-dependent transient reflectivity study. *Phys. Rev. B* **2020**, *101* (16), 165134.
50. Luo, H.; Greene, R. G.; Ruoff, A. L., beta -Po phase of sulfur at 162 GPa: X-ray diffraction study to 212 GPa. *Phys. Rev. Lett.* **1993**, *71* (18), 2943-2946.
51. Akahama, Y.; Kobayashi, M.; Kawamura, H., Pressure-induced structural phase transition in sulfur at 83 GPa. *Phys. Rev. B Condens. Matter.* **1993**, *48* (10), 6862-6864.
52. Sasaki, T.; Arai, M.; Furubayashi, T.; Matsumoto, T., Band-Structure Theory for the Insulating Phase of the Thio-Spinel Transition-Metal Compound, CuIr_2S_4 . *J. Phys. Soc. Jpn.* **2004**, *73* (7), 1875-1880.
53. Nobuhiro Matsumoto, S. N., Single-crystal growth of sulphospinel CuIr_2S_4 from Bi solution. *J. Cryst. Growth* **2000**, *210*, 772-776.
54. Sheldrick, G. M., SHELXT-Integrated space-group and crystal-structure determination. *Acta Crystallographica Section A: Foundations and Advances* **2015**, *71* (1), 3-8.
55. Bruker, A. P. E. X., *Saint and SADABS*. Bruker AXS Inc.: Madison, Wisconsin, USA, 2009.
56. Prescher, C.; Prakapenka, V. B., DIOPTAS: a program for reduction of two-dimensional X-ray diffraction data and data exploration. *High Pressure Research* **2015**, *35* (3), 223-230.
57. Toby, B. H.; Von Dreele, R. B., GSAS-II: the genesis of a modern open-source all purpose crystallography software package. *J. Appl. Crystallogr.* **2013**, *46* (2), 544-549.
58. Kresse, G.; Furthmüller, J., Efficiency of ab-initio total energy calculations for metals and semiconductors using a plane-wave basis set. *Comput. Mater. Sci.* **1996**, *6*, 15-50.
59. Kresse, G. a. J., D, From ultrasoft pseudopotentials to the projector augmented-wave method. *Phys. Rev. B* **1999**, *59*.
60. Perdew, J. P. a. B., Kieron and Ernzerhof, Matthias, Generalized Gradient Approximation Made Simple. *Phys. Rev. Lett.* **1996**, *77* (18), 3865-3868.

Insert Table of Contents artwork here

